

ANIMAL ROBOTS

A bipedal walking robot that can fly, slackline, and skateboard

Kyunam Kim^{1†}, Patrick Spieler^{1†}, Elena-Sorina Lupu¹, Alireza Ramezani^{1,2}, Soon-Jo Chung^{1,3*}

Numerous mobile robots in various forms specialize in either ground or aerial locomotion, whereas very few robots can perform complex locomotion tasks beyond simple walking and flying. We present the design and control of a multimodal locomotion robotic platform called LEONARDO, which bridges the gap between two different locomotion regimes of flying and walking using synchronized control of distributed electric thrusters and a pair of multijoint legs. By combining two distinct locomotion mechanisms, LEONARDO achieves complex maneuvers that require delicate balancing, such as walking on a slackline and skateboarding, which are challenging for existing bipedal robots. LEONARDO also demonstrates agile walking motions, interlaced with flying maneuvers to overcome obstacles using synchronized control of propellers and leg joints. The mechanical design and synchronized control strategy achieve a unique multimodal locomotion capability that could potentially enable robotic missions and operations that would be difficult for single-modal locomotion robots.

INTRODUCTION

Many of existing mobile robots use either ground locomotion or aerial locomotion, but not many of them are capable of both. Furthermore, only a few of these robots can perform complex locomotion tasks beyond simple walking and flying. In an effort to develop such a hybrid locomotion robot, this paper presents a multimodal locomotion robot called LEONARDO, or LEO for short, which is an acronym of LEgS ONboARd drOne (Fig. 1 and Movie 1). As the name suggests, the robot has two different locomotion mechanisms: multijoint legs and propeller-based thrusters, thereby achieving both terrestrial and aerial locomotion as well as the transition between walking and flying. The goal of LEO is twofold: (i) to enable robotic locomotion capabilities by leveraging its multimodality of flying and walking and (ii) to study the underlying robot design, dynamics, and control challenges of such a hybrid robotic platform, especially at the interface between walking, takeoff, and landing by using synchronous control of propellers and articulated joints.

Advantages and limitations of terrestrial robots

Numerous ground robots in various forms have been studied and developed over the past several decades, which may be categorized by their main locomotion methods: **legged** (1–4), **wheeled** (5–7), **rolling** (8–10), or **crawling** (11–13). Bipedal robots, in particular, have attracted great attention not only because of their human-like body shapes but also because they can perform versatile and robust walking, running, and jumping actions on uneven terrains (14, 15). Some advanced humanoid robots can even execute high-level tasks, such as object manipulation, ladder climbing, or driving a vehicle (16–19). However, the ultimate goal of bipedal robotics is to achieve human-like stability and robustness in its walking and running maneuvers over a challenging terrain or in a complex indoor environment. A great deal of research on bipedal robots exists in the literature, and

interested readers are referred to a survey work on this topic such as (3).

The safe mobility of ground robots is hindered by unfavorable ground conditions and the existence of obstacles of various sizes. This limits their practical applications to within well-structured environments such as indoor service robots (20, 21) or vacuum cleaners (22). Such limitations tend to necessitate that they are a highly engineered system with high development costs, as can be seen from some examples of space exploration rovers (23) or advanced humanoid robots (24). In addition, the applications of ground robots are restricted to movements that occur on or near the ground, because it can be challenging for them to gain access to an elevated location.

Advantages and limitations of aerial robots

The aforementioned difficulties can be overcome with aerial robots that fly over obstacles of any sizes or grounds of any conditions, and such robots have been another mainstream area of research in the robotics community. Both fixed-wing (25–27) and rotary-wing aircraft (28–30) as well as their hybrid types (31, 32) have been studied extensively and are proposed for real-world applications, such as remote sensing, delivery, search and rescue, surveillance, and real-time



Movie. 1. LEONARDO summary. The motivation and results of our study showing that the LEO robot performs a variety of locomotion maneuvers.

¹Division of Engineering and Applied Science, California Institute of Technology, 1200 E. California Boulevard, Pasadena, CA 91125, USA. ²Department of Electrical and Computer Engineering, Northeastern University, 360 Huntington Avenue, Boston, MA 02115, USA. ³Jet Propulsion Laboratory, California Institute of Technology, 4800 Oak Grove Drive, Pasadena, CA 91109, USA.

*Corresponding author. Email: sjchung@caltech.edu

†These authors contributed equally to this work.

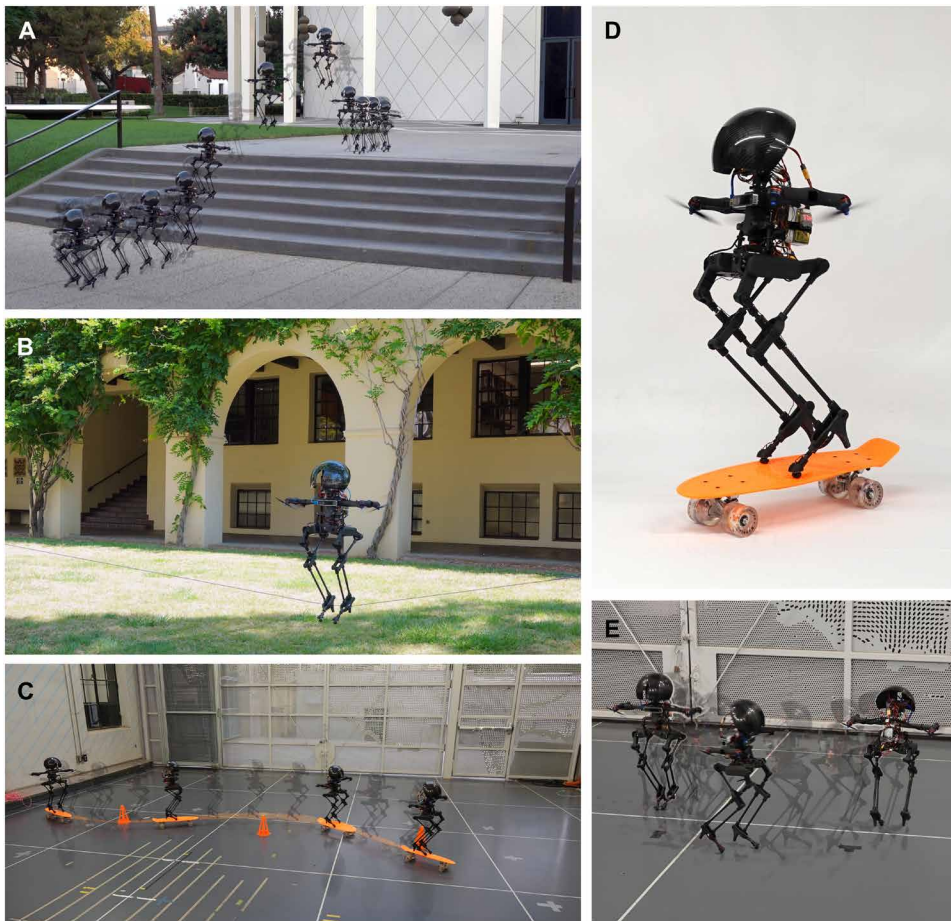


Fig. 1. LEO robot performing a variety of locomotion maneuvers. (A) Synchronized walking and flying maneuver to traverse stairs. (B) Balancing and walking on a slack rope stretched between two trees. (C) Riding on a skateboard around a series of obstacles. (D) Balancing on a skateboard. (E) Walking in a semicircle to show yawing movement capabilities.

monitoring (33). However, these robots come with their drawbacks, including large energy consumption, short flight and operation times, and limited onboard resources and payload weight. Furthermore, aerial robots have more difficulty than ground robots in physically interacting with their environment or other robots because they need to stabilize themselves in midair. Therefore, aerial robots have been mainly envisioned for applications that do not or minimally involve physical interactions, such as visual inspections, although aerial manipulation has recently become a popular research topic (34–37).

Multimodal locomotion and hybrid terrestrial and aerial robots

Robots with a multimodal locomotion ability have advantages over robots that have only a single mode of locomotion, such as moving through challenging environments by appropriately switching between available locomotion modes. However, the realization of such multimodal locomotion robots in practice has been a challenge. Further studies are needed to resolve the wide range of research issues, such as mechanical design, modeling and analysis, control system design, manufacturing, and experimental validation.

Whereas some previous works have presented terrestrial and aquatic locomotion abilities (38, 39), others have attempted to develop hybrid ground and aerial locomotion robots. Some of these robots adopt a fixed wing to take advantage of its endurance and efficiency combined with wheel legs (40) or whegs (41) to enable ground locomotion. Arguably, a challenge for these robots is to successfully transition from ground locomotion to flight by accelerating their forward speed to make their wing-borne lift force large enough for takeoff. Several approaches have been proposed to address this issue, including rooftop takeoff (42), gliding after jumping with spring-loaded legs (43), or adding propellers to enable vertical takeoff (44), at the expense of increased mechanical complexity.

To overcome the difficulty of ground-to-air transitions, hybrid locomotion robots using rotary wings for aerial locomotion have been developed. Although there has been an effort to invent a transformable robot that folds/unfolds a tail mechanism and rotor blades to fly similar to a helicopter (45), many prior works in this direction adopt a multirotor actuation mechanism. For example, the rolling cage (46) and the dynamic flying-walker (47) achieve ground locomotion with propeller thrust. However, the proposed designs exhibit limited versatility and adaptability on rough terrains. Others use actuated wheels (48, 49), because they are mechanically

simple, but they too have limited adaptability on complex terrains.

Some hybrid robot designs enable impressive locomotion maneuvers. For example, a quadrotor equipped with a climbing mechanism achieved the ability to perch on a wall from flying, climb up the wall, and take off from the wall to return to flying (50). In (51), a four-wheeled ground robot with two tiltable propellers demonstrated ground locomotion and wall climbing as well as the transitioning between the two. An interesting concept of a lighter-than-air flying robot with legs was proposed with the goal of improving bipedal walking stability using a helium-filled balloon, but its buoyancy was not sufficient for flying, and the robot was susceptible to wind (52).

Biological motivation for bimodal locomotion

Whereas bioinspired aerial robots (53–55) have been focused only on controlled flying maneuvers, terrestrial and aerial bimodal locomotion is a form of locomotion that is commonly found in animals such as insects, bats, and birds. Birds, in particular, fly to move a long distance to forage, to flee from predators, or to migrate for a better climate. Still, their multipurpose legs are what drove their evolutionary success because they enable multiple movement modalities

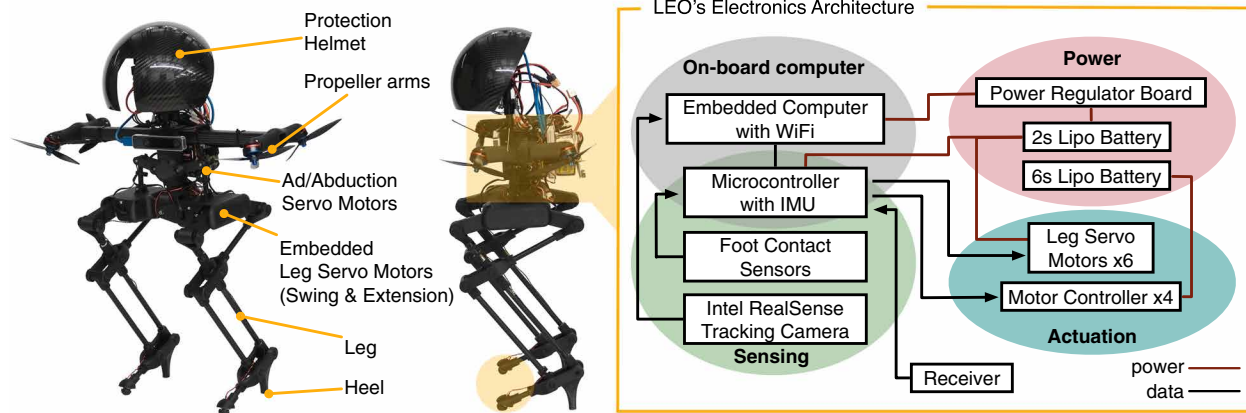


Fig. 2. Main electronics and mechanical components of LEO.

on the ground that are essential for **terrestrial foraging**, such as walking, running, jumping, resting, and perching (56).

A complex yet intriguing behavior happens at the transitional interface of the birds' two locomotion modes. Several robot designs have attempted to adopt the ideas and mechanisms from nature for their air-surface transitions (57). Furthermore, it is recognized in the literature that some birds use legs to provide a substantial amount of thrust for takeoff (58), which motivated and were applied to the development of the airplane (59). As such, one direction of studying bimodal locomotion robots is to take bioinspired approaches to facilitate their development based on scientific observations of birds. Moreover, bimodal locomotion robots have also been used to investigate the potential evolutionary process of bird locomotion (57). For instance, a hexapedal robot was appended with flapping wings not only to improve its running speed on the ground but also to provide an insight into the origin of bird flight (60).

Filling the gap between ground and aerial robots

LEO aims to bridge the gap between the two disparate domains of aerial and bipedal locomotion that are not typically intertwined in existing robotic systems. LEO targets versatile tasks that need to be accomplished in places that are difficult to reach by ground robots. Compared with a ground robot, **LEO can overcome any obstacle using the transition between its ground and flying modes** or easily reach an elevated location using propellers. In addition, whereas an aerial robot can hover over targets, LEO can use its ground locomotion to approach them for closer inspection. When LEO is in ground contact or walking, it can also reject large disturbances and prevent falling even on extremely slippery surfaces by using synchronized control of its distributed propellers and leg joints, thereby allowing for more robust and precise walking motion.

By leveraging its unique design and control concepts, LEO successfully demonstrates **walking and standing on a loosely tensioned rope** (Fig. 1B), a feature that is often seen in nature, as exhibited by birds walking on high-voltage or telephone lines. Furthermore, we demonstrate that LEO is capable of riding a passive wheeled skateboard, which is a nontrivial maneuver requiring a mastery of balancing even for humans, not to mention bipedal robots (Fig. 1C).

RESULTS

Robot system overview

LEO has a weight of **2.58 kg** and an overall height of **75 cm** when walking. LEO is composed of three main subsystems, namely, a torso, a propeller propulsion system, and two legs with point feet, as depicted in Fig. 2. LEO can operate completely autonomously with its onboard computers and sensor suite. The nominal walking speed of LEO is 20 cm/s, and its overall ground speed can substantially increase by using intermittent flying while close to the ground.

Legs and feet

The LEO legs are designed and built to be lightweight with a low moment of inertia, enabling agile walking and reducing the required propeller thrust to carry the legs as a payload during flight. To achieve this, the leg structures are constructed with carbon fiber tubes and three-dimensionally (3D) printed carbon fiber-reinforced nylon joints holding ball bearings. The **leg geometry** is designed to have **two closed kinematic loops**. This parallel mechanism allows the leg actuators to be **placed close to the torso**, resulting in a compact form with reduced leg inertia.

Both legs are symmetric, and **each leg has three servo motors** for actuation. The first one is located at the **pelvis** and moves the leg structure within the frontal plane of LEO. The other two servo actuators are located at the **front and back of the hip** and drive the **parallel leg mechanism** (see Fig. 3A). In combination, these two actuators drive the leg length and swing in a forward direction. The servo actuators driving the **legs of LEO are integrated brushless DC (BLDC) motors with high-reduction gearboxes and embedded position control**. The use of these integrated servo actuators minimizes the system size and weight, which are critical aspects for a flying robot. In addition, the embedded position controller is precise and fast enough for LEO's leg control due to the low inertia of the legs and the high bandwidth of the propeller controller that stabilizes the walking gait.

Regarding the design of the feet, there is a half-sphere of **polyurethane rubber** at the end of each leg, serving as a **point foot** with a high friction coefficient to prevent slipping during standing or walking. The half-sphere rubber foot sits **on top of an on/off switch**, which allows LEO to determine when **ground contact** is made during normal walking or when LEO switches its locomotion mode between walking and flying. Last, **heels** are installed such that LEO can **rest** on them without requiring active balancing, thereby allowing

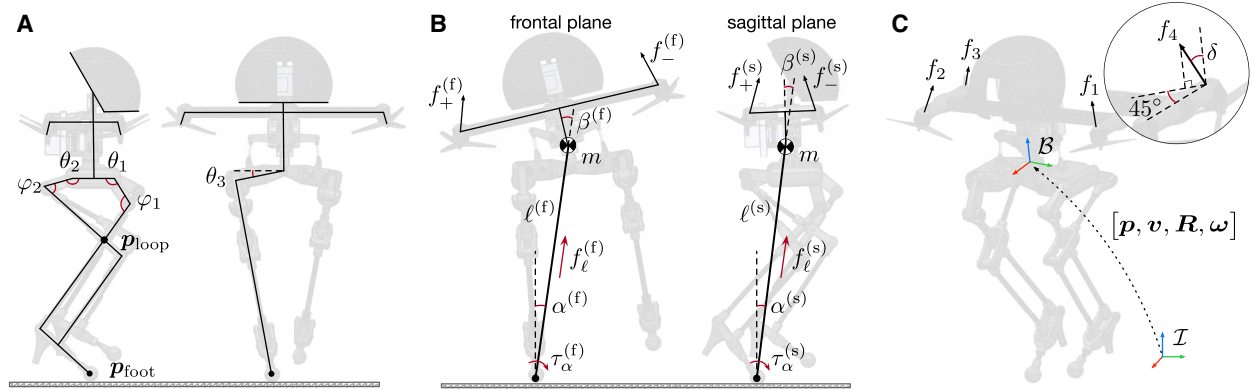


Fig. 3. The dynamical model of LEO. (A) Leg geometry with controlled joint angles θ_1, θ_2 , and θ_3 and passive joint angles φ_1 and φ_2 . (B) Planar IP model with propellers. Here, α^i with $i = \{(f), (s)\}$ is the angle between the virtual leg and the vertical axis, β^i is the torso angle with respect to the virtual leg, and ℓ^i is the length of the virtual leg. f_ℓ^i is the leg extension force, and τ_α^i is the moment about the pivot point generated by the lumped propeller thrusts f_+^i and f_-^i . (C) The body frame \mathcal{B} is fixed to the torso with the origin at the nominal CoM. Its location and orientation with respect to the inertial frame \mathcal{I} are given by \mathbf{p} and \mathbf{R} , respectively. Their time derivatives in the inertial frame are the linear and angular velocities \mathbf{v} and $\boldsymbol{\omega}$. The four controllable thrust forces f_1, \dots, f_4 are at a fixed tilt angle $\delta = 25^\circ$ with respect to the torso vertical axis. This tilt of the four thrust axes is directed inward at a 45° angle in the horizontal plane with respect to the forward direction. A vector description of the thrust axes is given in the Supplementary Text.

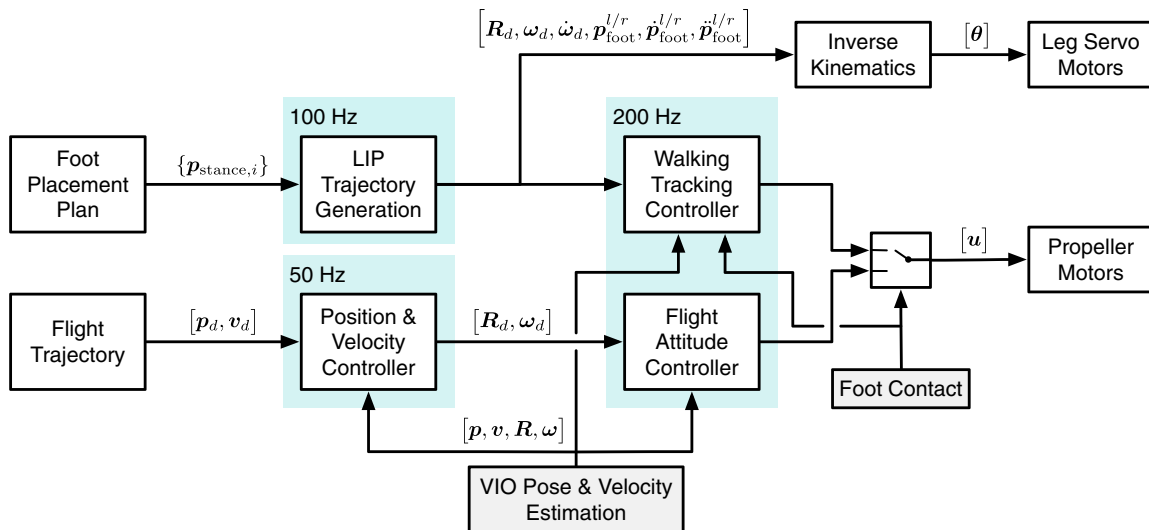


Fig. 4. Control architecture of LEO. The upper signal chain controls the walking mode, and the lower chain controls the flying mode. The propeller control is switched between these controllers based on the foot contact sensor measurements. $\mathbf{u} = [f_1, \dots, f_4]^T$ is the propeller thrust vector, $\boldsymbol{\theta}$ is the vector of servo joint angles for both legs, $\mathbf{p}_d, \mathbf{v}_d, \mathbf{R}_d$, and $\boldsymbol{\omega}_d$ are the desired position, velocity, attitude, and angular rate to be tracked. The vector $\mathbf{p}_{foot}^{l/r}$ contains the left and right foot positions. The list $\{p_{stance,i}\}$ contains a sequence of stance foot positions.

LEO to power down the propellers. When initiating normal walking, LEO raises itself from the lowered resting position on the heels. This motion lifts the heels to allow them to clear the ground during normal walking on a flat terrain.

Distributed propellers and motors

LEO has four symmetrically placed **propellers** at its shoulders, which are **used for stabilizing and controlling both the walking and flying** maneuvers. The propeller axes of rotation are selected to enable the generation of roll, pitch, and yaw moments in both positive and negative directions about the center of mass (CoM) for flying and about the current stance foot location for walking. Specifically, the **propeller axes are tilted by the angle of $\delta = 25^\circ$** inward from a

vertical axis (see Fig. 3C). Tilting the propeller thrust forces inward increases the moment the propellers can produce about the ground contact point, which improves the controllability for balancing and walking motions. However, there is a trade-off to be made, because larger tilt angles also reduce the net vertical thrust and flight efficiency. A further analysis of this trade-off can be found in the Supplementary Text. It is also possible to vary the tilt angles of the propellers with additional actuators while LEO is walking or flying to improve its performance. However, this was not done for LEO, because this feature would add extra weight and complexity. Each 6-inch-diameter unidirectional three-blade propeller has a fixed pitch, and its thrust is controlled via its rotation speed. The propellers are

directly driven by small BLDC motors, which are mounted on the arms fixed to the torso.

Torso design and electronics components

LEO's torso not only connects the arms and legs into one assembly but also houses onboard computers, sensors, and two lithium polymer (LiPo) batteries for powering the system (Fig. 2). LEO is equipped with two onboard computers. The first computer, a **NanoPC-T4**, has higher computational power and **runs Robot Operating System 2 to interface with sensors, receive commands, estimate states** based on sensor readings, and compute the desired trajectories. The second computer, a **microcontroller with a Real-Time Operating System**, **runs our nonlinear walking controller and the attitude flight controller at an update rate of 200 Hz**. It interfaces directly with the leg actuators and the propeller motor controller as well as an inertial measurement unit (IMU) for low-latency attitude information. The on/off switches embedded into the feet are used to detect foot-ground contact and are wired to the microcontroller.

Mass integration metric

The level of integration of a system having multiple modes of operation is quantitatively measured as the mass integration metric, denoted as I_{mass} , which is defined as the ratio of the summation of masses required to realize the modes without integration to the total integrated robot mass (61). It is defined for LEO as $I_{\text{mass}} = (m_{\text{fly}} + m_{\text{walk}})/m$ where m is the total mass of LEO, and m_{fly} and m_{walk} are the masses of the components of LEO associated with flying and walking, respectively. The metric $I_{\text{mass}} \in [1, 2]$, where 1 means no integration, and 2 means complete integration between the two modes. For LEO, the metric is computed as $I_{\text{mass}} = 1.39$, which shows that a moderate amount of LEO's components are shared for the two modes of locomotion.

Synchronized leg and propeller control

LEO's locomotion modes can be grouped into two main categories, ground and aerial locomotion, and each mode runs a dedicated feedback controller. The ground and aerial locomotion controllers are switched depending on the measured contact state of the two feet. LEO runs a state machine that ensures that these deliberate transitions occur reliably without switching back to the previous state even when the contact sensing is noisy (e.g., during landing). The walking controller further distinguishes between single and double stance phases, again based on the foot contact sensors.

All ground locomotion types (i.e., walking on the ground, skateboarding, walking on a slack rope, and balancing) make use of the same walking controller but with different input trajectories. In all these cases, the legs carry most of LEO's weight and control LEO's position by commanding the leg servo motors to follow joint angle trajectories derived from a walking gait trajectory. The propellers stabilize the walking gait by taking into account the foot positions and the foot contact states. This creates a synchronized control action between the legs and the propellers. Because the servo motors do not provide any feedback, the foot position estimates are taken from the reference trajectory.

For the flight mode, LEO is controlled as a standard quadrotor using only the four tilted propellers. An overview of the proposed controller architecture for LEO is shown in Fig. 4. In Materials and Methods, each component of this control architecture is elucidated in detail.

Experimental validation

We performed extensive testing of LEO in various scenarios to best show its versatile locomotion capabilities (see Fig. 1). Because of its

onboard stereo camera for localization, the robot can be tested both outdoors and indoors. These scenarios included walking on a flat terrain, synchronized flying and walking, and walking and balancing on a slack rope. In addition, we performed several experiments to showcase its high degree of maneuverability. For example, LEO was able to ride a skateboard around traffic cones by using the thrust of its propellers.

Thruster-aided ground locomotion

In this experiment, we demonstrated LEO's ground locomotion capability. The robot started from a resting position on its heels, with the propellers in an idle mode (Fig. 5A, i). In this mode, the propellers could also be turned off. LEO then stood up using its leg servo motors and, at the same time, used its propellers to balance (Fig. 5A, ii). Afterward, the robot started walking (Fig. 5A, ii to iv) and entered a periodic walking gait over the flat ground (Fig. 5A, v to viii).

The same experiment was repeated multiple times within a motion capture area to analyze the robot's motion. Note that the motion capture system was not used for feedback control; rather, it was used only to record the torso poses and the positions and orientations of both feet. The tracking data of 11 runs over a sequence of multiple steps are presented in Fig. 6 (A and B). In Fig. 6C, the trajectory of one of these runs is visualized in 3D.

The six plots in Fig. 6A show the left and right feet locations with respect to the CoM in the body axes. The dashed line marks the desired foot location. In all axes, we noticed some delay between the commanded and actual leg positions caused primarily by the limited tracking performance of the lightweight servo motors. We also observed that, particularly for the x axis, the delay increased slightly as soon as the leg touched the ground because the servo motors experienced more load.

Another aspect captured across the data in all axes is the leg deformation of the robot. In the y axis, the error increases whenever the robot is standing on the leg, especially for the left one. This error stems from the bending deformation of the leg structure in the frontal plane. In the z axis, there is an oscillation visible whenever the leg impacted the ground due to the overall elasticity of the leg structure. To reduce such leg deformation during walking, we commanded the propellers to generate a minimum thrust of 40% of the body weight to lessen the loads on the legs.

Figure 6B shows the walking trajectory tracking errors of the nonlinear controller in the sagittal and frontal planes. The details of the controller are presented in the subsection below titled "Nonlinear tracking controller for walking using propellers." The frontal tracking has a root mean square (RMS) error of 2.6° median across all the runs. In contrast, the sagittal tracking error is lower, with a median RMS error of 1.6° . This difference occurs because the frontal plane controller has lower feedback gains than the sagittal one, because the legs were more flexible in that direction, which induced unwanted oscillations for higher gains. Another experiment was performed to demonstrate the yawing movement capability of LEO as depicted in Fig. 1E and movie S1, where LEO was tracking a semi-circle trajectory, and the yaw control was achieved using propellers.

Robustness to external disturbances on the ground

To further demonstrate LEO's strong robustness to external disturbances, additional experiments were performed. In the first experiment, LEO used the nonlinear tracking controller with a constant attitude setpoint standing upright on one leg, and it was pushed with a stick multiple times in the sagittal and frontal planes, as seen in Fig. 7B. The robot successfully rejected the disturbances, as presented

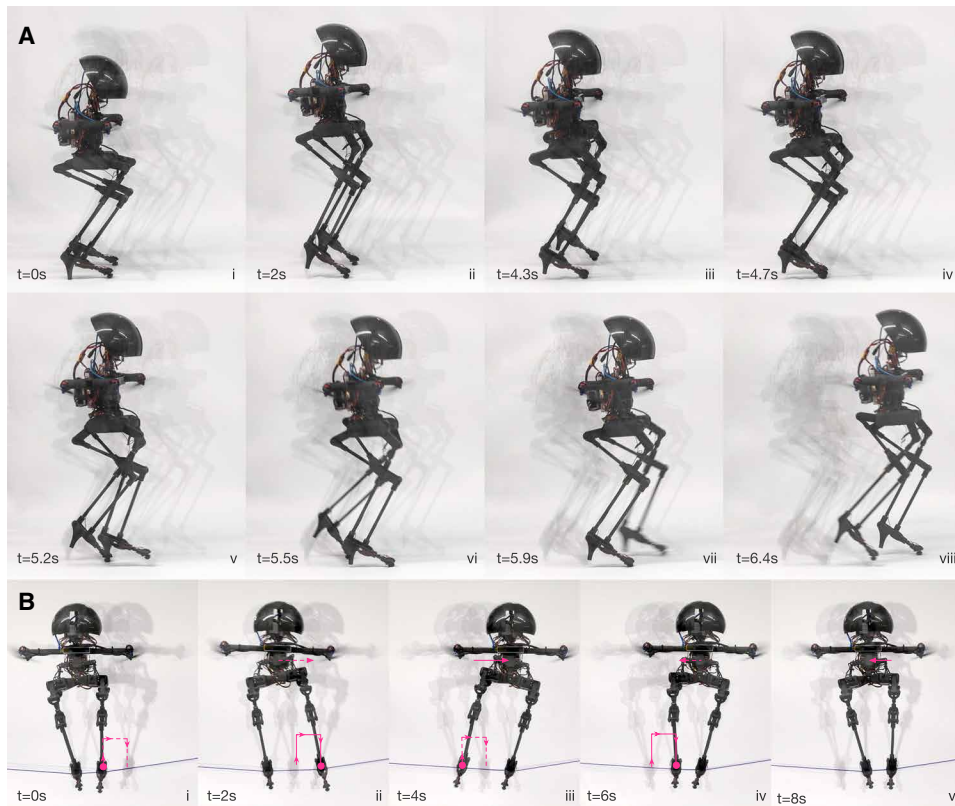


Fig. 5. Walking sequences. (A) LEO standing up from its resting position on the heels and starting a periodic walking gait. (B) LEO traversing a flexible rope. Dashed arrows indicate the movement from the current to the next snapshot in sequence, and solid arrows show the executed movement since the previous snapshot.

in the top plot of Fig. 7A by applying the thrusts shown in the bottom plot. Movie S2 shows this experiment and the same experiment repeated on a slippery surface (a whiteboard with added oil), where LEO starts sliding when disturbances are applied, but it does not lose balance.

The ground locomotion experiments were mainly focused on flat terrain conditions. The main limitation with walking on a highly rough terrain comes from the limited range of motion of the legs, not the stability of the controller. The current leg kinematics design of LEO allows for about 4 cm of ground clearance; thus, traversing rough terrain cannot be achieved safely with this leg geometry. An improved leg design that allows a more extensive range of leg motions and more ground clearance should allow LEO to walk over rough terrain by leveraging the stabilization capability of propellers. With the current design, however, LEO can still overcome the rough terrain by flying over it.

To compare LEO's disturbance rejection capability with a flying vehicle, we placed both LEO balancing on one leg on a rigid table and a standard commercial drone in front of a wind tunnel. We then switched on the wind tunnel to a speed of 3.8 m/s. The drone was immediately blown back at this wind speed, but LEO could withstand this disturbance thanks to the frictional ground contact (see movie S3). This demonstrates that LEO is more resistant to wind when it is in contact with a rigid surface.

Synchronized walking and flying

In this experiment, we showcase LEO's capability to combine walking and flying to overcome obstacles. We performed the experiment

in an indoor laboratory environment with the robot tethered for safety precautions (Fig. 7D and movie S4). Two tables were placed about 1 m apart, and LEO traversed them by flying over the gap. LEO followed a predefined trajectory because the stereo camera was not used to detect the gap or the tables but only provided navigation information to the robot. We present the actual and desired positions and velocities of LEO together with the propeller thrusts in Fig. 7C. LEO transitioned from walking to flying by increasing its collective propeller thrust until both feet lost ground contact ($t = 8$ s). At that point, an upward velocity was initiated, and LEO climbed away from the ground. Then, the robot followed a smooth flying trajectory up to the landing point. The forward landing velocity was matched to the predetermined walking speed, and the walking phase was again triggered when one foot touched the ground. After the touchdown, the robot continued to walk on the second table. In addition, a similar experiment was performed without the safety tether, flying down from a single table, as shown in movie S5.

We also validated the synchronized walking and flying control by performing outdoor experiments where LEO flew down a set of stairs, as seen in movie S6.

A sequence of images overlaid to form a single image showing this motion is illustrated in Fig. 1A. This experiment demonstrates that LEO can execute controlled maneuvers that combine walking, take-off, flying, and landing with smooth transitions between flying and walking gaits.

Thruster-aided balancing and walking on a slackline

Inspired by the fact that birds can walk and balance on a loosely tensioned rope, we designed several experiments to show LEO's balancing and walking capabilities on an elastic rope stretched between two trees (Fig. 1B). The rope was placed along the arch of LEO's feet. LEO was able to balance and walk sideways successfully using the same nonlinear balancing controller used for walking on the ground. However, in this configuration, the feet contact sensors cannot detect when the robot was standing on the rope. Therefore, we overrode the feet contact sensors and feet position information in the controller with a fixed virtual foot contact centered just underneath the robot. The controller was robust enough to perform well, although the actual foot location and contact states are different from the controller estimates.

A sequence of images showing LEO walking sideways on the rope is displayed in Fig. 5B. The walking trajectory is a periodic sequence, which alternates between shifting the CoM from one leg to another (Fig. 5B, ii to iii and iv to v) and advancing a leg (Fig. 5B, i to ii and iii to iv). In this trajectory, the CoM is always kept above the stance foot or line connecting the two feet in a double stance phase. The position of the robot, tracking error, and the generated

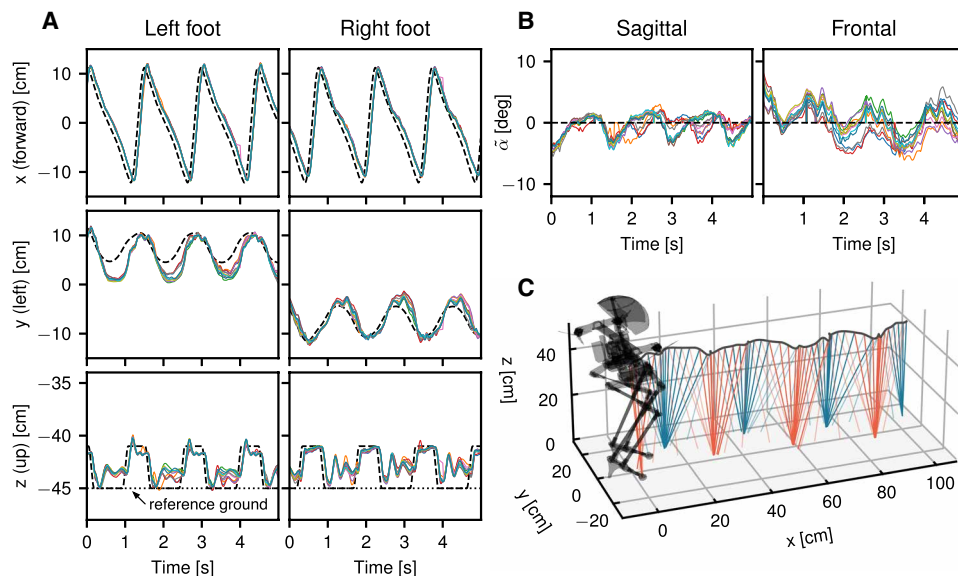


Fig. 6. LEO walking at 0.2 m/s over flat ground. (A) Left and right feet positions tracked by a motion capture system for 11 runs. The coordinates are in a forward-left-up body frame with respect to the CoM. The dashed lines are the reference foot trajectories. In the z-axis plot, the ground level of the reference trajectory is shown as a dotted line. The deviations of the foot trajectories from the reference ground level during stance phases are caused by compression of the leg, which manifests as an offset because the foot position is plotted relative to the CoM. (B) Tracking errors of our nonlinear controller in sagittal and frontal planes, $\tilde{\alpha}^{(s)}$ and $\tilde{\alpha}^{(f)}$, for the same runs (see Fig. 3 for a free-body diagram of LEO). (C) 3D visualization of a single run. The line segments connect foot positions to CoM position at regular time intervals. The transparent line segments indicate that the foot sensor detects no contact.

thrust from the propellers are plotted in fig. S1 in the Supplementary Materials. A movie of the experiment can be found in movie S6.

Riding a passive skateboard

In this experiment, LEO was riding on a passive skateboard. The skateboard controller used the same nonlinear walking controller as in the previously mentioned experiments, because this controller can track arbitrary body and leg orientations using control of distributed propellers. Riding the skateboard was decoupled into two control problems: controlling the steering angle and controlling the skateboard's forward acceleration/deceleration. On a skateboard, steering is achieved by tilting the board around its longitudinal axis. This, in turn, rotates the skateboard's wheel axis, which is mounted on an angled, spring-loaded joint. We placed LEO on the skateboard with its feet spaced apart in the lateral direction. An extension of its legs tilted the skateboard and allowed steering.

The forward acceleration was achieved by moving the CoM of the robot backward while simultaneously pitching the body forward. When in a steady state, the controller applied a moment that canceled the gravitational moment of the off-centered CoM to maintain balance in this state. This moment was realized with the rear propellers generating more thrust, which resulted in the robot and the skateboard being pushed forward. Deceleration is achieved in an opposite fashion by leaning forward and pitching its body backward. This method ignores the transients of moving the body into the leaning positions during which reverse forces would be produced, thereby limiting the control bandwidth. However, this controller was adequate for direct manual control.

One result of experimentation is shown in Fig. 1C and in movie S8, where LEO rode on the skateboard and slalomed around a series

of traffic cones. LEO was driven manually via a remote control by directly controlling the desired acceleration and steering angle. In this composite image (Fig. 1C), a snapshot is taken at every 1.5 s. The figure shows the robot during the acceleration phase in the beginning, the deceleration phase in the end, and the steering phase when the skateboard is tilted.

Control input signals during walking and flying

As a hybrid walking-flying robot, it is important for LEO to have a sufficient amount of control authority both on the ground and in the air. Specifically, LEO's propellers must be able to provide sufficient moments in all three axes for balancing when walking and for attitude control when flying, while guaranteeing that a desired range of thrust is attainable as the moment and thrust capabilities are coupled together. If the desired thrust and moments computed from the controller require the propellers to generate thrusts exceeding their limit, saturation will occur, which could lead to control system failure. In addition, if friction or normal force constraints during ground locomotion are

not met, the robot could start sliding or take off. To verify that our choice of LEO's design parameters provides sufficient control capability, we investigate control input signals from our experiments and compare them with LEO's control capability.

Figure 8 shows control input signals in terms of net vertical thrust and moments during LEO's walking and flying and the attainable moment sets of LEO under different conditions. Figure 8A was obtained while LEO performed several steps on a flat ground, and Fig. 8B presents the flight phase of the table-to-table experiment (Fig. 7D).

Figure 8A (i) shows that the net vertical thrust from the propellers remains less than the total weight of LEO during walking, thereby preventing the loss of contact. In Fig. 8B (i), the net vertical thrust is greater than LEO's weight during the initial takeoff from the table and then stays at around the value equal to the weight for maintaining the height.

The magnitudes of the horizontal thrust forces due to the propeller tilt are shown in Fig. 8A (ii) for walking and in Fig. 8B (ii) for flying. Despite a somewhat large propeller tilt angle, the vertical component is the dominant of the net thrust while flying, and we exploit this when we allocate control efforts to the four propellers during flying in the section below titled "Determinacy of control allocation."

Figure 8C shows the attainable moment sets of LEO with respect to the stance foot. The outermost set $\mathcal{T}_{f_z < mg}^{\text{walk}}$ is the maximum attainable moment set when the resultant net vertical thrust f_z ranges from 0 to 100% of the body weight. The inner sets $\mathcal{T}_{f_z}^{\text{walk, no-slip}}$ are the sets that are constrained such that f_z is equal to the denoted values, and the stance foot does not slip with the measured friction

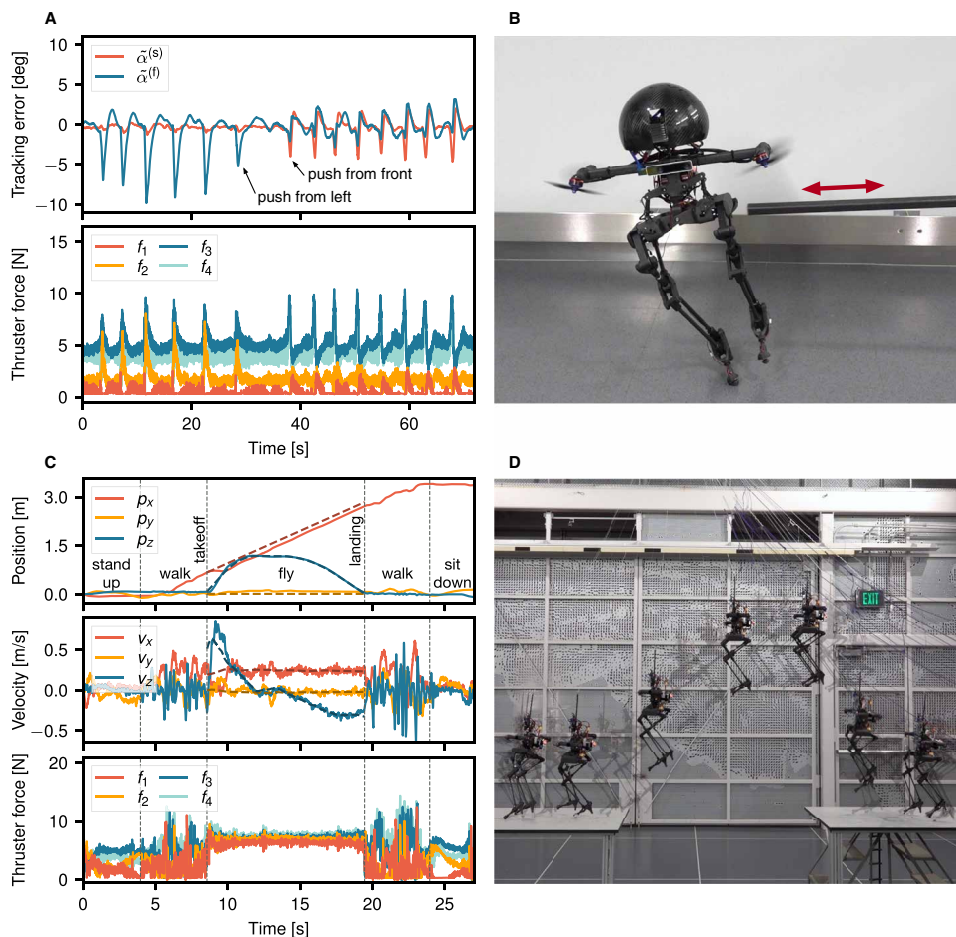


Fig. 7. Disturbance rejection and synchronized walking and flying experiments for LEO. (A) Perturbation rejection experiment. The top plot shows the tracking error in both the sagittal and frontal planes during a series of 14 applied perturbations. The bottom plot presents the commanded thrust force of each of the four propellers. (B) Picture of LEO being pushed externally with a stick. (C) Trajectory plots of LEO performing a synchronized walking and flying maneuver to traverse two tables. The first two plots show the robot's actual position and velocity, together with the desired position and velocity (dashed line) for the flight phase. The third plot shows the commanded propeller thrust. (D) Overlaid snapshots of LEO performing the synchronized walking and flying experiment, tethered for safety.

coefficient of 0.84. The formal definitions of these sets are discussed in the section below titled “Constrained/unconstrained attainable moment sets.” As can be seen from Fig. 8D, the size of $\mathcal{T}_{f_z}^{\text{walk, no-slip}}$ increases as f_z increases up to a certain point, and then it starts to decrease once the no-slip conditions are activated due to the decreased ground normal force. The roll and pitch dimensions of the set shrink to null when f_z is equal to the body weight, at which point no friction force is possible on the stance foot.

The moment sets for flying are shown in Fig. 8E. Because the effective moments are computed about the CoM of LEO in this case instead of the ground contact point, the size of the maximum attainable moment set \mathcal{T}^{fly} is smaller than $\mathcal{T}^{\text{walk}}$ due to the shortened moment arm.

Figure 8A (iii to v) shows the roll, pitch, and yaw moment control signals, respectively, during walking, together with their bounds. The bounds are computed from the attainable moment sets constrained by f_z applied at each time step, and there are two types of

bounds used: $\mathcal{T}_{f_z}^{\text{walk, no-slip}}$ that considers no-slip conditions and $\mathcal{T}_{f_z}^{\text{walk}}$ that does not. Note that the moment set $\mathcal{T}_{f_z}^{\text{walk, no-slip}}$ is a subset of $\mathcal{T}_{f_z}^{\text{walk}}$, and there are several time instances when the moment control signals belong to the latter but not to the former. When this happens, the moments are attainable only by violating the no-slip conditions, which implies instantaneous slips, but LEO was able to maintain the balance at these instances using propeller control. Figure 8B (iii to v) shows that the moment signals for flying are well bounded by their respective bounds computed from $\mathcal{T}_{f_z}^{\text{fly}}$ at each time instant.

DISCUSSION

LEO's position as a multimodal locomotion robot

Recently, robots using both propellers and legs, similar to LEO, have been proposed in the literature. For instance, the monopedal robot in (62) was initially built as an agile vertical jumping robot, but later, two thrusters were added (63, 64) to control its attitude in midair to enable multiple high-precision jumps in series. Another robot with four propellers and two legs has been introduced with the goal of demonstrating a walking appearance, which was referred to as pseudo-locomotion, for entertainment purposes (65). Although the configuration of the proposed robot is similar to that of LEO, this robot mainly uses propellers, not legs, for its movement, and its multimodal locomotion ability has not been demonstrated. In (66), a pair of coaxial propellers were added to a bipedal robot to assist its stable walking,

and hence, the work was not focused on investigating multimodal locomotion aspects, especially for takeoff and landing maneuvers.

It might appear as though the designs of the aforementioned robots shared a robot concept similar to LEO; however, we note that the design philosophies that these robots were based on are fundamentally different from each other because of their clearly different objectives. Specifically, the robot in (65) was not designed for dynamic walking, and its design and control did not consider the robot's interaction with the ground. In addition, the robot in (64) focused only on precision robotic hopping, whereas the robot in (66) was designed only for bipedal walking, and hence, their propellers were not intended for flight maneuvers. On the other hand, LEO's design enables dynamic bipedal walking with complex ground interaction while preserving the flight performance of a multirotor vehicle. Therefore, we believe that LEO truly integrates bipedal locomotion with flying. LEO demonstrated that synchronized propeller control greatly improves the stability of inherently unstable

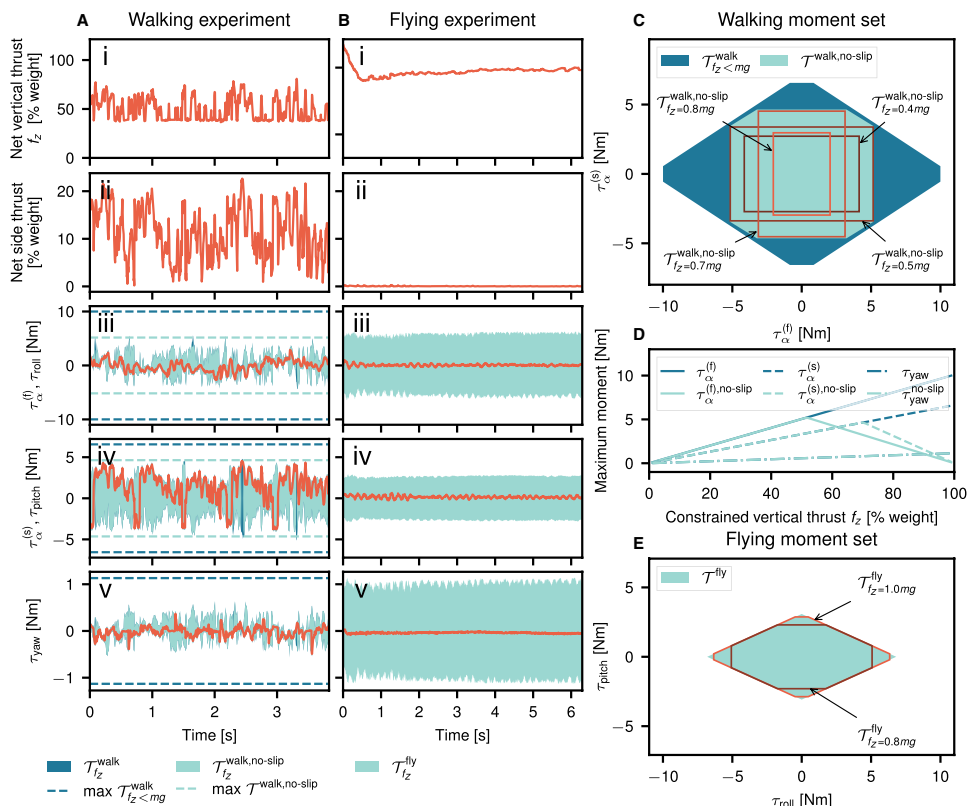


Fig. 8. Commanded thrust and moment signals and attainable moment sets during walking and flying experiments. (A and B) Thrust and moment signals for walking and flying experiments, respectively. (A and B) (i) Net upward (in the body frame) thrust from all propellers. (A and B) (ii) Net side (in body frame) thrust from all propellers. (A) (iii) to (v) Commanded moments $\tau_{\alpha}^{(f)}$, $\tau_{\alpha}^{(s)}$, τ_{yaw} during walking. The light and dark shaded areas mark the moment set constrained to the instantaneous net vertical thrust f_z with and without the no-slip constraint, respectively. Also shown are the maximum/minimum bounds (dashed line) of the moment set with and without the no-slip constraint. (B) (iii) to (v) Commanded moments τ_{roll} , τ_{pitch} , τ_{yaw} during flying. The shaded area marks the moment set constrained to the instantaneous vertical thrust f_z . (C) Moment sets in walking mode. (D) Maximum moments in walking mode as a function of vertical thrust with and without the no-slip constraint. (E) Moment sets in flying mode.

bipedal walking even within extreme scenarios in which other bipedal robots usually fail, such as walking on a rope. Furthermore, successfully riding a wheeled skateboard can be regarded as LEO's achieving of an additional type of locomotion modality.

Energy efficiency and cost of transportation of LEO

The extreme balancing ability of LEO comes at the cost of continuously running propellers, which leads to higher energy consumption than legs-only ground robots. However, this stabilization with propellers allowed the use of low-power leg servo motors and lightweight legs with flexibility, which was a design choice to minimize the overall weight of LEO to improve its flying performance.

We note that the optimization of LEO's energy consumption was not a priority in this work. However, we investigated its cost of transportation (CoT), a dimensionless quantity characterizing the energy efficiency of locomotion. It is defined as $CoT := \frac{P}{mgv}$, where P is the power consumption of the robot whose mass is m while moving with a constant velocity v measured at the standard gravitational acceleration g . For LEO, the measured CoT was 108 when walking at a speed of 20 cm/s. When flying at 1 m/s, the CoT was 48, and it

decreased to 15.5 at the flight speed of 3 m/s. Further information on the energy consumption and a comparison with other biological systems and robots are provided in the Supplementary Text.

There are possible ways to improve the energy efficiency by making different design trade-offs. For instance, LEO with more rigid legs would require less thrust for preventing excessive leg deformation. Furthermore, LEO could walk with the reduced support from the propellers by adopting finite feet for better stability or higher power motors with torque control for joint actuation that would allow for fast and accurate enough foot position tracking to stabilize the walking gait. In such a case, propellers may need to turn on only when the legs fail to maintain stability on the ground without having to run continuously. These solutions would cause a weight increase and lead to a higher energy consumption during flight maneuvers, but they would lower energy consumption during walking. In the case of LEO, we aimed to achieve balanced aerial and ground locomotion capabilities, and we opted for lightweight legs. Achieving efficient walking with lightweight legs similar to LEO's is still an open challenge in the field of bipedal robots, and it remains to be investigated in future work.

Potential applications

By leveraging LEO's hybrid locomotion capability, it is anticipated that LEO will enable a wide range of robotic missions that are hard to accomplish by the sole

use of ground or aerial robots. Perhaps the most well-suited applications for LEO would be the ones that involve physical interactions with structures at a high altitude, which are usually dangerous for human workers and call for a substitution by robotic workers. In such applications, conventional bipedal robots have difficulties with reaching the site, and standard multirotor drones have an issue with stabilization in high-disturbance environments. LEO uses the ground contact to its advantage and, compared with a standard multirotor, is more resistant to external disturbances such as wind (movie S3), which would improve the safety of the robot operation in an outdoor environment where LEO can maintain contact with a rigid surface.

Specifically, multipoint inspection, repair, or replacement tasks at locations that are difficult to reach by humans could be one primary application domain for LEO. For example, high-voltage line inspection is currently done by highly skilled professionals who not only inspect the lines from a distance but also walk on the lines to inspect and repair them. If the lines are in hard-to-reach places, helicopters bring workers close to the lines. Instead of sending humans, LEO could fly up to the high-voltage lines and walk on them for close-by inspection and repair, which could potentially reduce

fatalities and cost of the task. Another good application for LEO would be painting of tall bridges. Currently, workers walk on slippery and sometimes round trusses for painting, and their risk of slipping is high. We believe that LEO is a good substitution of human workers for this task because LEO can maintain balance on slippery terrain (movie S2) and because it can choose to fly to a safe location in case it falls. Similarly, LEO can be envisioned for other tasks such as inspection of a building roof or pipes of an oil refinery.

On the other hand, the technology developed for LEO's transition between ground and aerial locomotion modes could foster the development of adaptive landing gear systems composed of controlled leg joints for aerial robots and other types of flying vehicles (67, 68). Such legged landing gear systems would be especially useful for maintaining body balance of aerial robots while landing on sloped or uneven terrains, thereby reducing the risk of failure under harsh landing conditions.

MATERIALS AND METHODS

In this section, the individual components of the control architecture of LEO from Fig. 4 are detailed. We emphasize the kinematics and dynamics models used for generating walking trajectories and discuss our control strategy for walking and flying as well as the transition between the two. An in-depth analysis of the control authority of LEO's actuation mechanism is also provided.

Inverted pendulum model for the walking phase of LEO

A controller based on an inverted pendulum (IP) model is chosen for LEO's walking because it captures the robot's fundamental dynamics (see Fig. 3B). This model assumes the following: All the masses are concentrated at a single point mass inside the torso, the legs are massless, and the stance foot acts as a pivot with the ground. These are reasonable assumptions because LEO's legs are lightweight, with all the actuators and electronics located in the torso. The model is further simplified by considering the frontal and sagittal planes separately; hence, the dynamics prescribing LEO's ground locomotion are represented in two 2D planes instead of one 3D space. In addition to a conventional IP model, we add propellers that are used to stabilize the dynamics. These thrust forces serve as the only control input in this model.

Walking trajectory generation with linear IP model

If the height of the CoM is kept constant by controlling the leg extension force, the dynamic model of IP becomes linear in a Cartesian coordinate parameterization. This model is called linear IP (LIP) (69) and was used for LEO's walking trajectory generation. Because we constrain the CoM to be at a constant height, this reference trajectory has no discontinuity in the vertical velocity from the impulsive ground reaction force due to impacts from leg exchange, which also leads to no discontinuities in the horizontal velocity. This model and the reference trajectory simplify the controller design, as explained further below in the "Nonlinear tracking controller for walking using propellers" subsection.

Our approach of designing the walking trajectory closely follows (69), which exploits the linearity of the model to find closed-form solutions for foot placements and CoM trajectories. Although simple in formulation, versatile walking patterns are possible with this method by modifying walking characteristics through different choices of a step period, a step length, or a desired CoM height. Because of

the simplicity of this approach, the trajectories can be easily computed online.

We modify the LIP model with the addition of a constant uniform thrust from all four propellers to reduce the weight on the legs. By setting the torso attitude level ($\beta^i = \alpha^i$), with $i \in \{(s), (f)\}$ corresponding to the sagittal and frontal planes, respectively, we find that the constant propeller thrust f_z enters the dynamics as a reduced gravitational acceleration

$$\ddot{x} = \frac{g - f_z/m}{z}x \quad (1)$$

Here, the x and z coordinates are the forward and vertical positions of the CoM with respect to the stance foot location, and g is the gravitational acceleration. This planar model is also valid in the frontal plane with y instead of x . The resulting trajectory looks natural, with the CoM swinging from side to side as the robot makes steps. These trajectories require only the chosen constant thrust to be followed, minimizing the control action needed. The swing leg trajectory is parameterized such that it lifts and sets the foot down vertically and moves in between stance locations in a straight line.

Leg joint trajectory generation

Once the feet and CoM trajectories are designed, the relative foot trajectories are transformed into the associated joint angle trajectories to be tracked by a set of servo motors. This requires solving the inverse kinematics problem of the leg chain. Within the workspace of the legs, there is a unique feasible joint configuration for any foot position, which makes the inverse kinematics a well-posed problem. We solve the inverse kinematics by first finding θ_3 (Fig. 3) in the frontal plane analytically and then numerically solving for θ_1 and θ_2 by finding the solution of the following function

$$\begin{bmatrix} \mathbf{p}_{\text{foot}}^d - \mathbf{p}_{\text{foot}}(\theta_1, \theta_2, \varphi_1, \varphi_2) \\ \mathbf{p}_{\text{loop}_1}(\theta_1, \varphi_1) - \mathbf{p}_{\text{loop}_2}(\theta_2, \varphi_2) \end{bmatrix} = \mathbf{0}$$

where $\mathbf{p}_{\text{foot}}^d$ is the desired foot position in the plane of the parallel leg mechanism. We overparameterize the kinematics problem with the additional angles φ_1 and φ_2 , and we add a constraint that the point \mathbf{p}_{loop} is the same from both sides of the kinematic chain, i.e., $\mathbf{p}_{\text{loop}_1} = \mathbf{p}_{\text{loop}_2}$. This results in much simpler expressions compared with an analytic solution of \mathbf{p}_{loop} based on θ_1 and θ_2 only, which speeds up the computation. Note that the second kinematic loop is a parallelogram, which makes the computation of \mathbf{p}_{foot} as a function of \mathbf{p}_{loop} and the angles θ_1 , θ_2 , φ_1 , and φ_2 straightforward. Assuming feasibility, the angles are found using the Levenberg-Marquardt (LM) algorithm. We use the LM implementation in the nonlinear optimization module of Eigen library (70), which runs fast enough to be used online. Although the LM is a local method, it converges to the correct solution using a neutral leg configuration as an initial guess.

Modeling of IP for propeller control during stance phase

A diagram of the considered model is shown in Fig. 3B. Conceptually, as previously mentioned, this model can be seen as a projection of a full 3D model onto the frontal or sagittal plane. In this model, LEO's configuration is parameterized by the link length ℓ and the angle α between the virtual leg (the line segment connecting the CoM to the stance foot) and the inertial vertical axis on each plane. Thus, we define the vector of generalized coordinates as $\mathbf{q}^i := [\ell^i, \alpha^i]^T$ (i.e., $\mathbf{q}^i = \mathbf{q}^{(s)}$ or $\mathbf{q}^i = \mathbf{q}^{(f)}$).

Using the Lagrangian method, the equations of motion for this model can be put in the following Euler-Lagrange form

$$\mathbf{M}^i(\mathbf{q}^i) \ddot{\mathbf{q}}^i + \mathbf{C}^i(\mathbf{q}^i, \dot{\mathbf{q}}^i) \dot{\mathbf{q}}^i + \mathbf{G}^i(\mathbf{q}^i) = \begin{bmatrix} f_\ell^i \\ \tau_\alpha^i \end{bmatrix} \quad (2)$$

where

$$\mathbf{M}^i = \begin{bmatrix} m & 0 \\ 0 & m(\ell^i)^2 \end{bmatrix}, \mathbf{C}^i = \begin{bmatrix} 0 & -m\ell^i \dot{\alpha}^i \\ m\ell^i \dot{\alpha}^i & m\ell^i \dot{\ell}^i \end{bmatrix}, \mathbf{G}^i = \begin{bmatrix} mg \cos(\alpha^i) \\ -mg \ell^i \sin(\alpha^i) \end{bmatrix}$$

and f_ℓ^i is the leg extension force along the virtual leg, and τ_α^i is the moment generated by the propeller thrusts f_+^i and f_-^i about the pivot point. Note that β^i does not contribute to the model, although in reality, this angle is controlled by the leg servo motors, which have a limited bandwidth. Therefore, we do not assume control of β^i for stabilization.

Nonlinear tracking controller for walking using propellers

We present a nonlinear integral controller for walking using propellers, which guarantees exponential convergence of the angle α^i to a desired trajectory α_d^i obtained from Eq. 1. We use the IP model presented in the previous section restricted to one coordinate (α^i) because we assume that the servo motors embedded in the legs are tracking the leg angle (β^i) and length (ℓ^i). Unlike in the ideal case of the planned LIP trajectory, impacts can occur in our IP model when the foot exchange did not happen at the planned time because of tracking errors or uneven terrains. However, these impacts can be regarded as a disturbance in the controller's nonlinear stability analysis. LEO's nonlinear tracking controller with a sufficiently high gain achieves exponential convergence of tracking errors to the bounded balls around the impact-less desired trajectory before the next leg exchanges. Note that because this controller stabilizes the planar model, two instantiations are run to control the sagittal and frontal plane individually.

Several factors can potentially yield modeling errors such as the CoM offset, inaccurate thruster models, structural deformation, or gearbox backlash. We noticed that the largest error arises from the CoM offset, which we model as a bounded external torque τ_{ext} . To compensate for this torque, we implement a nonlinear integral tracking controller with feedforward cancellation (71, 72) for each angle $\alpha^i = \alpha^{(f)}$ or $\alpha^i = \alpha^{(s)}$ as

$$\tau_\alpha^i = m(\ell^i)^2 \ddot{\alpha}_r^i + 2m\ell^i \dot{\ell}^i \dot{\alpha}^i - mg\ell^i \sin(\alpha^i) - k^i(\alpha^i - \alpha_r^i) - k_\ell^i \int_{t_0}^t (\alpha^i(\xi) - \alpha_r^i(\xi)) d\xi \quad (3)$$

where α_r^i is the reference angular velocity defined as $\dot{\alpha}_r^i = \dot{\alpha}_d^i - k_\alpha^i \bar{\alpha}^i$, with an error angle $\bar{\alpha}^i = \alpha^i - \alpha_d^i$. The parameters k_α^i , k^i , and k_ℓ^i are positive scalar gains, and t_0 and t are the initial and current time steps, respectively. The adaptive term (i.e., integral term in Eq. 3) ensures exponential convergence to the desired trajectory with the following error ball in the presence of an external disturbance term with the bounded time derivative $\dot{\tau}_{\text{ext}}^i(t)$

$$\lim_{t \rightarrow \infty} \int_0^{\bar{\alpha}^i} \|\delta \bar{\alpha}^i\|_2 \leq \eta(m, \ell^i(t), k_P^i, k^i, k_\alpha^i) \sup_t \|\tau_{\text{ext}}^i(t)\|_2 \quad (4)$$

which indicates that the size of the error ball only depends on $\sup_t \|\tau_{\text{ext}}^i\|_2$, not $\|\tau_{\text{ext}}^i\|_2$. Also note that this error bound is valid only in the regime between impacts because they are not explicitly modeled.

Proof: The expression of η together with the proof of exponential convergence and the error ball derivation are presented in the Supplementary Text.

Heading controller for walking

LEO's heading is controlled using propellers. Because LEO's feet form point contacts with the ground, the robot is free to rotate in all three axes, including yaw, when only one foot is in ground contact. In this case, the propellers can be used to control the heading of the robot using a proportional-integral-derivative controller. The controller outputs a yaw moment that is mixed with the desired pitch and roll moments from the walking tracking controllers.

Optimized control allocation for walking

Once the desired control moments are computed, they are mixed to get propeller motor signals. Let $\tau_d = [\tau_\alpha^{(f)}, \tau_\alpha^{(s)}, \tau_{\text{yaw}}]$, where the first two elements of the torque vector are computed from Eq. 3 and the last element from the previously mentioned heading controller, and let f_i be the thrust force from the i th propeller and denote its magnitude as f_i (i.e., $f_i = \|f_i\|_2$). The control effectiveness matrix $\mathbf{B}^{\text{walk}} \in \mathbb{R}^{3 \times 4}$ maps individual propeller thrusts to the moments about the stance foot. To compute the propeller thrusts that yield the desired control moments, we solve the following optimization problem for $\mathbf{u} = [f_1, \dots, f_4]^T$

$$\begin{aligned} & \underset{\mathbf{u}}{\text{argmin}} \quad \|\mathbf{u}\|_1 \\ & \text{subject to} \quad \mathbf{B}^{\text{walk}} \mathbf{u} = \tau_d \\ & \quad 0 \leq f_{\min} \leq f_i, i = 1, \dots, 4 \\ & \quad f_z^d / \cos(\delta) \leq \|\mathbf{u}\|_1 \end{aligned} \quad (5)$$

Each propeller thrust f_i is constrained to be greater than the idle thrust f_{\min} , which is based on the minimum rotation speed at which the sensorless BLDC controllers can run the motors. The last inequality enforces a minimum desired collective upward thrust f_z^d , which is used to reduce weight on the legs. Note that Eq. 5 always has a solution because the rows of \mathbf{B}^{walk} are linearly independent, and there exists a \mathbf{u}^+ strictly positive element-wise such that $\mathbf{B}^{\text{walk}} \mathbf{u}^+ = \mathbf{0}$, which is given by the geometry of our tilted propeller axes. The optimization problem is solved using a closed-form solution given in the Supplementary Text. In case the allocation results in thrust forces f_i that exceed the maximum thrust, they are truncated. However, such a situation was not observed in our experiments. This allocation scheme does not consider friction or normal force constraints. However, our experiments presented in Fig. 8 and the discussion in the "Control input signals during walking and flying" subsection show that these constraints are usually met in practice.

Flight controller

In a flight mode, LEO uses a position and attitude controller similar to (31). Specifically, the desired angular rate is computed from the attitude error between the current and desired body orientation. Then, the desired control moments are computed in roll, pitch, and yaw directions from the angular rate error. Last, the control moments and the desired thrust are mixed to compute propeller motor

signals, where the desired thrust is computed from position and velocity errors. Note that in this case, the propeller moments are computed with respect to the CoM, not about the stance foot because it no longer serves as a pivot point.

Transition between walking and flying

As explained earlier, the selection of the active controller (flying or walking) depends on whether the foot contact sensors detect the ground or not (see Fig. 4). Takeoff and landing are achieved by generating suitable walking and flying trajectories and monitoring the foot contact state to switch between them. During takeoff, the collective propeller thrust f_z^d from Eq. 5 is increased while LEO is walking until the ground contact is lost. Then, a flight trajectory with an initial upward velocity is initiated, which allows LEO to quickly lift away from the ground. LEO executes its desired flight trajectory thereafter.

For landing, LEO enters a constant velocity descent until one of the foot contact sensors detects the ground. During this descent, the legs are in a configuration that allows the robot to switch to walking immediately. Once the ground contact is detected, the flying trajectory is aborted, and the flight attitude controller is given a zero thrust and a level attitude setpoint. Furthermore, the walking gait with the same speed as the forward velocity of the descent is initiated. This allows for a seamless transition from flying to walking.

Determinacy of control allocation

LEO's controller is designed to switch between the two control allocation schemes depending on its current locomotion choice determined by the inputs from the foot sensors. When LEO is walking on the ground, four propellers are used to stabilize its attitude with the three moments they generate, and hence, the control effectiveness matrix \mathbf{B}^{walk} from Eq. 5 has one more column than its number of rows. Without the inequality constraints, the system defined with the equality constraint only in Eq. 5 is underdetermined, and the solution \mathbf{u} may not be unique, which is why the control allocation problem is formulated as an optimization problem in Eq. 5.

On the other hand, the effective matrix becomes square when LEO is flying because the wrench $\tau_d^{\text{fly}} = [\tau_{\text{roll}}, \tau_{\text{pitch}}, \tau_{\text{yaw}}, f_z]^T$ is now a 4D vector composed of three moments and one collective vertical thrust, which is realized by four propellers. In this case, either a unique solution \mathbf{u} exists and is solved for a given τ_d^{fly} by inverting the effective matrix $\mathbf{B}^{\text{fly}} \in \mathbb{R}^{4 \times 4}$, or no solution exists if the inequality constraints cannot be satisfied. Because the allocation has to find \mathbf{u} at every time step in the control loop, a relaxed solution is returned in the latter case by setting, for example, the components f_i of \mathbf{u} that are saturated to the allowed minimum or maximum values, respectively. The solution \mathbf{u} returned by this ad hoc approach, however, does not yield a correct τ_d^{fly} , and the control performance may degrade if this truncation persists for extended periods. The best way to avoid this saturation issue is to investigate the attainable control set and design it such that the desired control inputs are well bounded within the set during LEO's operation. This property of LEO is investigated in Fig. 8.

Strictly speaking, the wrench generated by the action of propellers is a 6D vector (three moments and three forces) because horizontal thrust forces are also generated by the tilted propellers as they run, in addition to the components of the 4D wrench τ_d^{fly} above. In this case, the effectiveness matrix \mathbf{B}^{fly} is a six-by-four matrix, and the control allocation becomes an overdetermined system, implying

that there usually does not exist a solution. For this reason, we ignored the rows of the effectiveness matrix corresponding to the horizontal thrust forces and treated it as a square matrix in the above discussion. This choice is justified by the fact that the horizontal thrust forces are smaller than the vertical ones. Furthermore, most of the horizontal thrust forces are canceled out due to the symmetry of propeller locations and orientations when LEO is performing gentle flying maneuvers, as illustrated in Fig. 8B (ii).

Constrained/unconstrained attainable moment sets

As mentioned in the "Control input signals during walking and flying" subsection, the attainable moment sets should be sufficiently large to avoid saturation of propellers and to find proper solutions to the control allocation problem. To investigate this issue, the concept of attainable moment sets is formally defined here.

We define the attainable moment set \mathcal{T} of LEO as the set of all moments that can be generated by the propellers, namely, $\mathcal{T} = \{\tau \in \mathbb{R}^3 \mid f_{\min} \leq f_i \leq f_{\max}, \forall i \in \{1, \dots, 4\}\}$, where f_{\min} and f_{\max} represent the lower and upper limits of the propeller forces, and τ is the sum of individual moments from the four propellers whose expression is given in detail in the Supplementary Text. The set \mathcal{T} is a polyhedron in a 3D space as depicted in Fig. 8. For LEO to be attitude-controllable during its balancing, walking, or flying, the origin must be strictly inside \mathcal{T} , and it is desirable to have a large neighborhood around the origin to maximize the ability to generate a moment in any direction (73). Recall that the reference point for moment calculation is different for walking and flying phases. To distinguish between the two cases, we use a superscript, e.g., $\mathcal{T}^{\text{walk}}$ and \mathcal{T}^{fly} , when necessary.

Although the set \mathcal{T} characterizes the moment control input used for attitude control, it does not consider the resultant thrust $\mathbf{f} = \sum_{i=1}^4 \mathbf{f}_i$ associated with $\tau \in \mathcal{T}$. Because the net vertical thrust f_z plays an important role for LEO's control, we choose to constrain \mathcal{T} with f_z as $\mathcal{T}_{f_z} = \{\tau \in \mathbb{R}^3 \mid \sum_{i=1}^4 f_{i,z} = f_z, f_{\min} \leq f_i \leq f_{\max}\}$, where $f_{i,z}$ is the component of \mathbf{f}_i in the body z axis. Note that the constrained attainable moment set \mathcal{T}_{f_z} is different for the walking and flying cases even if f_z is the same, which we distinguish as $\mathcal{T}_{f_z}^{\text{walk}}$ and $\mathcal{T}_{f_z}^{\text{fly}}$.

During LEO's walking, f_z is used to determine whether the stance foot maintains ground contact. Therefore, $\mathcal{T}_{f_z}^{\text{walk}}$ is defined as the union of the sets $\mathcal{T}_{f_z < mg}^{\text{walk}} = \{\cup \mathcal{T}_{f_z}^{\text{walk}} \mid f_z < mg\}$. In addition, we introduce a no-slip attainable moment set in the "Control input signals during walking and flying" subsection and in Fig. 8 as the set of attainable moments without the occurrence of the stance foot slipping. For this, we inspect the net horizontal thrust and the static friction cone. Using the linearized friction cones, we define the no-slip attainable moment set as $\mathcal{T}_{f_z}^{\text{walk, no-slip}} = \{\tau \in \mathbb{R}^3 \mid \sum_{i=1}^4 f_{i,z} = f_z, f_{\min} \leq f_i \leq f_{\max}, |f_{rx}| \leq \eta_s f_{rz}, |f_{ry}| \leq \eta_s f_{rz}, f_{rz} \geq 0\}$, where η_s is the linear static friction coefficient, and $\mathbf{f}_r = [f_{rx}, f_{ry}, f_{rz}]^T$ is the ground reaction force at the stance foot. A detailed derivation of the no-slip conditions is presented in the Supplementary Text.

Estimation of torso orientation

LEO is equipped with an Intel RealSense T265 camera that integrates onboard visual inertial odometry (VIO) processing. This sensor provides the position and orientation as well as the linear and angular velocity of the torso-fixed body frame \mathcal{B} with respect to the gravity-aligned inertial reference frame \mathcal{I} (Fig. 3C). During walking, the controller uses the leg angle α^i in both the sagittal and frontal planes, as well as yaw heading as a state parametrization. The $\alpha^{(s)}$

and $\alpha^{(f)}$ angles are computed from the position of the foot in ground contact with respect to the torso and the torso attitude projected in the sagittal and frontal planes. For flying, we rely on the position from the VIO for localization, which requires good visual features for the robot's operation. However, for walking control, we only rely on the estimation of attitude from the VIO, which is robust even in the presence of a small number of visual features.

SUPPLEMENTARY MATERIALS

www.science.org/doi/10.1126/scirobotics.abf8136

Supplementary Text

Sections S1 to S7

Figs. S1 to S3

Tables S1 and S2

Movies S1 to S8

References (74–79)

REFERENCES AND NOTES

1. M. H. Raibert, *Legged Robots that Balance* (MIT Press, 1986).
2. U. Asif, J. Iqbal, On the improvement of multi-legged locomotion over difficult terrains using a balance stabilization method. *Int. J. Adv. Robot. Syst.* **9**, 1 (2012).
3. J. W. Grizzle, C. Chevallereau, R. W. Sinnet, A. D. Ames, Models, feedback control, and open problems of 3D bipedal robotic walking. *Automatica* **50**, 1955–1988 (2014).
4. D. J. Hyun, S. Seok, J. Lee, S. Kim, High speed trot-running: Implementation of a hierarchical controller using proprioceptive impedance control on the MIT Cheetah. *Int. J. Robot. Res.* **33**, 1417–1445 (2014).
5. J.-M. Yang, J.-H. Kim, Sliding mode control for trajectory tracking of nonholonomic wheeled mobile robots. *IEEE Trans. Robot. Autom.* **15**, 578–587 (1999).
6. F. Tâche, W. Fischer, G. Caprari, R. Siegwart, R. Moser, F. Mondada, Magnebike: A magnetic wheeled robot with high mobility for inspecting complex-shaped structures. *J. Field Robot.* **26**, 453–476 (2009).
7. R. P. M. Chan, K. A. Stol, C. R. Halkyard, Review of modelling and control of two-wheeled robots. *Annu. Rev. Control.* **37**, 89–103 (2013).
8. S. Bhattacharya, S. K. Agrawal, Spherical rolling robot: A design and motion planning studies. *IEEE Trans. Robot. Autom.* **16**, 835–839 (2000).
9. V. A. Joshi, R. N. Banavar, R. Hippalgaonkar, Design and analysis of a spherical mobile robot. *Mech. Mach. Theory* **45**, 130–136 (2010).
10. K. Kim, A. K. Agogino, A. M. Agogino, Rolling locomotion of cable-driven soft spherical tensegrity robots. *Soft Robot.* **7**, 346–361 (2020).
11. A. Crespi, A. Badertscher, A. Guignard, A. J. Ijspeert, AmphiBot I: An amphibious snake-like robot. *Robot. Auton. Syst.* **50**, 163–175 (2005).
12. A. Hoover, E. Steltz, R. Fearing, RoACH: An autonomous 2.4g crawling hexapod robot, in *Proceedings of the IEEE/RSJ International Conference on Intelligent Robots and Systems*, Nice, France, 22 to 26 September 2008, pp. 26–33.
13. R. F. Shepherd, F. Ilievski, W. Choi, S. A. Morin, A. A. Stokes, A. D. Mazzeo, X. Chen, M. Wang, G. M. Whitesides, Multigait soft robot. *Proc. Natl. Acad. Sci. U.S.A.* **108**, 20400–20403 (2011).
14. E. R. Westervelt, J. W. Grizzle, C. Chevallereau, J. H. Choi, B. Morris, *Feedback Control of Dynamic Bipedal Robot Locomotion* (CRC Press, 2018).
15. C. Hubicki, A. Abate, P. Clary, S. Rezazadeh, M. Jones, A. Peekema, J. Van Why, R. Domres, A. Wu, W. Martin, H. Geyer, J. Hurst, Walking and running with passive compliance: Lessons from engineering: A live demonstration of the ATRIAS biped. *IEEE Robot. Autom. Mag.* **25**, 23–39 (2018).
16. M. Johnson, B. Shrewsbury, S. Bertrand, T. Wu, D. Duran, M. Floyd, P. Abeles, D. Stephen, N. Mertins, A. Lesman, J. Carff, W. Rifenburg, P. Kaveti, W. Straatman, J. Smith, M. Griffioen, B. Layton, T. de Boer, T. Koolen, P. Neuhaus, J. Pratt, Team IHMC's lessons learned from the DARPA robotics challenge trials. *J. Field Robot.* **32**, 192–208 (2015).
17. S. Feng, E. Whitman, X. Xinjilefu, C. G. Atkeson, Optimization-based full body control for the DARPA robotics challenge. *J. Field Robot.* **32**, 293–312 (2015).
18. H. A. Yanco, A. Norton, W. Ober, D. Shane, A. Skinner, J. Vice, Analysis of human-robot interaction at the DARPA robotics challenge trials. *J. Field Robot.* **32**, 420–444 (2015).
19. J. Lim, I. Lee, I. Shim, H. Jung, H. M. Joe, H. Bae, O. Sim, J. Oh, T. Jung, S. Shin, K. Joo, M. Kim, K. Lee, Y. Bok, D.-G. Choi, B. Cho, S. Kim, J. Heo, I. Kim, J. Lee, I. S. Kwon, J.-H. Oh, Robot system of DRC-HUBO+ and control strategy of team KAIST in DARPA Robotics Challenge finals. *J. Field Robot.* **34**, 802–829 (2017).
20. R. Triebel, K. O. Arras, R. Alami, L. Beyer, S. Breuers, R. Chatila, M. Chetouani, D. Cremers, V. Evers, M. Fiore, H. Hung, O. A. I. Ramirez, M. Joosse, H. Khambhaita, T. Kucner, B. Leibe, A. J. Lilienthal, T. Linder, M. Lohse, M. Magnusson, B. Okal, L. Palmieri, U. Rafi, M. van Rooij, L. Zhang, SPENCER: A socially aware service robot for passenger guidance and help in busy airports, in *Proceedings of the 10th Conference on Field and Service Robotics* (2015), vol. 113, pp. 607–622.
21. M. Veloso, J. Biswas, B. Coltin, S. Rosenthal, CoBots: Robust symbiotic autonomous mobile service robots, in *Proceedings of the 24th International Conference on Artificial Intelligence* (2015), pp. 4423–4429.
22. J. Geringer, R. Watson, J. Cooper, Robot vacuum cleaner (2010).
23. J. P. Grotzinger, J. Crisp, A. R. Vasavada, R. C. Anderson, C. J. Baker, R. Barry, D. F. Blake, P. Conrad, K. S. Edgett, B. Ferdowski, R. Gellert, J. B. Gilbert, M. Golombek, J. Gómez-Elvira, D. M. Hassler, L. Jandura, M. Litvak, P. Mahaffy, J. Maki, M. Meyer, M. C. Malin, I. Mitrofanov, J. J. Simmonds, D. Vaniman, R. V. Welch, R. C. Wiens, Mars Science Laboratory mission and science investigation. *Space Sci. Rev.* **170**, 5–56 (2012).
24. G. Nelson, A. Saunders, R. Playter, The PETMAN and Atlas robots at Boston Dynamics, in *Humanoid Robotics: A Reference* (2019), pp. 169–186.
25. J.-C. Zufferey, A. Klapotcz, A. Beyeler, J.-D. Nicoud, D. Floreano, A 10-gram vision-based flying robot. *Adv. Robot.* **21**, 1671–1684 (2007).
26. H. J. Kim, M. Kim, H. Lim, C. Park, S. Yoon, D. Lee, H. Choi, G. Oh, J. Park, Y. Kim, Fully autonomous vision-based net-recovery landing system for a fixed-wing UAV. *IEEE/ASME Trans. Mechatron.* **18**, 1320–1333 (2013).
27. X. Shi, P. Spieler, E. Tang, E.-S. Lupu, P. Tokumaru, S.-J. Chung, Adaptive nonlinear control of fixed-wing VTOL with airflow vector sensing, in *Proceedings of the IEEE International Conference on Robotics and Automation (ICRA)* (2020), pp. 5321–5327.
28. B. Crowther, A. Lanzon, M. Maya-Gonzalez, D. Langkamp, Kinematic analysis and control design for a nonplanar multirotor vehicle. *J. Guid. Control. Dyn.* **34**, 1157–1171 (2011).
29. R. Mahony, V. Kumar, P. Corke, Multirotor aerial vehicles: Modeling, estimation, and control of quadrotor. *IEEE Robot. Autom. Mag.* **19**, 20–32 (2012).
30. D. Brescianini, R. D'Andrea, An omni-directional multirotor vehicle. *Mechatronics* **55**, 76–93 (2018).
31. X. Shi, K. Kim, S. Rahili, S.-J. Chung, Nonlinear control of autonomous flying cars with wings and distributed electric propulsion, in *Proceeding of the IEEE Conference on Decision and Control (CDC)*, Miami, FL, 17 to 19 December 2018, pp. 5326–5333.
32. C. De Wagter, R. Ruijsink, E. J. Smeur, K. G. van Hecke, F. van Tienen, E. van der Horst, B. D. Remes, Design, control, and visual navigation of the DeltaCopter VTOL tail-sitter UAV. *J. Field Robot.* **35**, 937–960 (2018).
33. H. Shakhatareh, A. H. Sawalmeh, A. Al-Fuqaha, Z. Dou, E. Almaita, I. Khalil, N. S. Othman, A. Kheirshah, M. Guizani, Unmanned aerial vehicles (UAVs): A survey on civil applications and key research challenges. *IEEE Access* **7**, 48572–48634 (2019).
34. G. Heredia, A. Jimenez-Cano, I. Sanchez, D. Llorente, V. Vega, J. Braga, J. Acosta, A. Ollero, Control of a multirotor outdoor aerial manipulator, in *Proceedings of the IEEE/RSJ International Conference on Intelligent Robots and Systems*, Chicago, IL, 14 to 18 September 2014, pp. 3417–3422.
35. F. Ruggiero, M. Trujillo, R. Cano, H. Ascorbe, A. Viguria, C. Perez, V. Lippiello, A. Ollero, B. Siciliano, A multilayer control for multirotor UAVs equipped with a servo robot arm, in *Proceedings of the IEEE International Conference on Robotics and Automation (ICRA)*, Seattle, WA, 26 to 30 May 2015, pp. 4014–4020.
36. S. Kim, H. Seo, H. J. Kim, Operating an unknown drawer using an aerial manipulator, in *Proceedings of the IEEE International Conference on Robotics and Automation (ICRA)*, Seattle, WA, 26 to 30 May 2015, pp. 5503–5508.
37. H.-N. Nguyen, S. Park, J. Park, D. Lee, A novel robotic platform for aerial manipulation using quadrotors as rotating thrust generators. *IEEE Trans. Robot.* **34**, 353–369 (2018).
38. G. Dudek, P. Giguere, C. Prahacs, S. Saunderson, J. Sattar, L.-A. Torres-Mendez, M. Jenkin, A. German, A. Hogue, A. Ripsman, J. Zacher, E. Milios, H. Liu, P. Zhang, M. Buehler, C. Georgiades, Aqua: An amphibious autonomous robot. *Computer* **40**, 46–53 (2007).
39. A. J. Ijspeert, A. Crespi, D. Ryczko, J.-M. Cabelguen, From swimming to walking with a salamander robot driven by a spinal cord model. *Science* **315**, 1416–1420 (2007).
40. R. J. Bachmann, R. Vaidyanathan, R. D. Quinn, Drive train design enabling locomotion transition of a small hybrid air-land vehicle, in *Proceedings of the IEEE/RSJ International Conference on Intelligent Robots and Systems*, St. Louis, MO, 10 to 15 October 2009, pp. 5647–5652.
41. L. Daler, J. Lecoeur, P. B. Hählen, D. Floreano, A flying robot with adaptive morphology for multi-modal locomotion, in *Proceedings of the IEEE/RSJ International Conference on Intelligent Robots and Systems*, Tokyo, Japan, 3 to 7 November (2013), pp. 1361–1366.
42. F. J. Boria, R. J. Bachmann, P. G. Ifju, R. D. Quinn, R. Vaidyanathan, C. Perry, J. Wagener, A sensor platform capable of aerial and terrestrial locomotion, in *Proceedings of the IEEE/RSJ International Conference on Intelligent Robots and Systems*, Edmonton, AB, 2 to 6 August 2005, pp. 3959–3964.
43. M. Kovač, J.-C. Zufferey, D. Floreano, Towards a self-deploying and gliding robot, in *Flying Insects and Robots* (Springer, 2009), pp. 271–284.
44. L. Daler, thesis, École polytechnique fédérale de Lausanne, Lausanne, Switzerland (2015).
45. A. Kossett, N. Papanikolopoulos, A robust miniature robot design for land/air hybrid locomotion, in *Proceedings of the IEEE International Conference on Robotics and Automation*, Shanghai, China, 9 to 13 May 2011, pp. 4595–4600.

46. A. Kalantari, M. Spenko, Design and experimental validation of HyTAQ, a hybrid terrestrial and aerial quadrotor, in *Proceedings of the IEEE International Conference on Robotics and Automation*, Karlsruhe, Germany, 6 to 10 May 2013, pp. 4445–4450.
47. C. J. Pratt, K. K. Leang, Dynamic underactuated flying-walking (DUCK) robot, in *Proceedings of the IEEE International Conference on Robotics and Automation*, Stockholm, Sweden, 16 to 21 May 2016, pp. 3267–3274.
48. S. Morton, N. Papanikolopoulos, A small hybrid ground-air vehicle concept, in *Proceedings of the IEEE/RSJ International Conference on Intelligent Robots and Systems (IROS)*, Vancouver, BC, 24 to 28 September 2017, pp. 5149–5154.
49. H. Wang, J. Shi, J. Wang, H. Wang, Y. Feng, Y. You, Design and modeling of a novel transformable land/air robot. *International Journal of Aerospace Engineering* **2019**, 1–10 (2019).
50. M. T. Pope, C. W. Kimes, H. Jiang, E. W. Hawkes, M. A. Estrada, C. F. Kerst, W. R. Roderick, A. K. Han, D. L. Christensen, M. R. Cutkosky, A multimodal robot for perching and climbing on vertical outdoor surfaces. *IEEE Trans. Robot.* **33**, 38–48 (2016).
51. P. Beardsley, R. Siegrwart, M. Arigoni, M. Bischoff, S. Fuhrer, D. Krummenacher, D. Mammolo, R. Simpson, Vertigo—a wall-climbing robot including ground-wall transition, 2015; <https://la.disneyresearch.com/publication/vertigo/> [Online; accessed 22 September 2021].
52. S. Ghassemi, D. Hong, Feasibility study of a novel robotic system BALLU: Buoyancy assisted lightweight legged unit, in *Proceedings of the 16th IEEE International Conference on Humanoid Robots (Humanoids)*, Cancun, Mexico, 15 to 17 November 2016, pp. 144–144.
53. K. Y. Ma, P. Chirarattananon, S. B. Fuller, R. J. Wood, Controlled flight of a biologically inspired, insect-scale robot. *Science* **340**, 603–607 (2013).
54. A. A. Paranjape, S.-J. Chung, J. Kim, Novel dihedral-based control of flapping-wing aircraft with application to perching. *IEEE Trans. Robot.* **29**, 1071–1084 (2013).
55. A. Ramezani, S.-J. Chung, S. Hutchinson, A biomimetic robotic platform to study flight specializations of bats. *Sci. Robot.* **2**, eaal2505 (2017).
56. A. Abourachid, E. Höfling, The legs: A key to bird evolutionary success. *J. Ornithol.* **153**, 193–198 (2012).
57. W. R. Roderick, M. R. Cutkosky, D. Lentink, Touchdown to take-off: At the interface of flight and surface locomotion. *Interface Focus* **7**, 20160094 (2017).
58. K. D. Earls, Kinematics and mechanics of ground take-off in the starling *Sturnis vulgaris* and the quail *Coturnix coturnix*. *J. Exp. Biol.* **203**, 725–739 (2000).
59. E. Ackerman, Delivery drones use bird-inspired legs to jump into the air, 2019. [Online; accessed 6 November 2020].
60. K. Peterson, P. Birkmeyer, R. Dudley, R. Fearing, A wing-assisted running robot and implications for avian flight evolution. *Bioinspir. Biomim.* **6**, 046008 (2011).
61. M. A. Woodward, M. Sitti, Multimo-bat: A biologically inspired integrated jumping-gliding robot. *Int. J. Robot. Res.* **33**, 1511–1529 (2014).
62. D. W. Haldane, M. M. Plecnik, J. K. Yim, R. S. Fearing, Robotic vertical jumping agility via series-elastic power modulation. *Sci. Robot.* **1**, eaag2048 (2016).
63. D. W. Haldane, J. K. Yim, R. S. Fearing, Repetitive extreme-acceleration (14-g) spatial jumping with Salto-1P, in *Proceedings of the IEEE/RSJ International Conference on Intelligent Robots and Systems (IROS)*, Vancouver, BC, 24 to 28 September 2017, pp. 3345–3351.
64. J. K. Yim, B. R. P. Singh, E. K. Wang, R. Featherstone, R. S. Fearing, Precision robotic leaping and landing using stance-phase balance. *IEEE Rob. Autom. Lett.* **5**, 3422–3429 (2020).
65. A. Maekawa, R. Niiyama, S. Yamanaka, Pseudo-locomotion design with a quadrotor-assisted biped robot, in *Proceedings of the IEEE International Conference on Robotics and Biomimetics (ROBIO)*, Kuala Lumpur, 12 to 15 December 2018, pp. 2462–2466.
66. P. Dangol, A. Ramezani, N. Jalili, Performance satisfaction in Harpy, a thruster-assisted bipedal robot. arXiv:2004.14337 (2020).
67. J. Kiefer, M. Ward, M. Costello, Rotorcraft hard landing mitigation using robotic landing gear. *J. Dyn. Syst. Meas. Control.* **138**, 031003 (2016).
68. Y. S. Sarkisov, G. A. Yashin, E. V. Tsykunov, D. Tsetserukou, Dronegear: A novel robotic landing gear with embedded optical torque sensors for safe multicopter landing on an uneven surface. *IEEE Rob. Autom. Lett.* **3**, 1912–1917 (2018).
69. S. Kajita, H. Hirukawa, K. Harada, K. Yokoi, *Introduction to Humanoid Robotics* (Springer, 2014).
70. G. Guennebaud, B. Jacob, Eigen v3 2010; <http://eigen.tuxfamily.org> [Online; accessed 11 December 2020].
71. H. K. Khalil, *Nonlinear Systems* (Prentice-Hall, ed. 2, 1996).
72. J. E. Slotine, W. Li, *Applied Nonlinear Control* (Prentice-Hall, 1991).
73. K. Kim, S. Rahili, X. Shi, S.-J. Chung, M. Gharib, Controllability and design of unmanned multirotor aircraft robust to rotor failure, in *AIAA Scitech 2019 Forum* (2019).
74. A. V. Tucker, Energetic cost of locomotion in animals. *Comp. Biochem. Physiol.* **34**, 841–846 (1970).
75. N. Kau, A. Schultz, N. Ferrante, P. Slade, Stanford Doggo: An open-source, quasi-direct-drive quadruped, in *Proceedings of the IEEE International Conference on Robotics and Automation* (2019), pp. 6309–6315.
76. J. P. Reher, A. Hereid, S. Kolathaya, C. M. Hubicki, A. D. Ames, Algorithmic foundations of realizing multi-contact locomotion on the humanoid robot DURUS, in *Algorithmic Foundations of Robotics XII* (2020), pp. 400–415.
77. S. Bandyopadhyay, S.-J. Chung, F. Y. Hadaegh, Nonlinear attitude control of spacecraft with a large captured object. *J. Guid. Control. Dyn.* **39**, 754–769 (2016).
78. W. Lohmiller, J.-J. E. Slotine, On contraction analysis for non-linear systems. *Automatica* **34**, 683–696 (1998).
79. B. W. McCormick, *Aerodynamics, Aeronautics, and Flight Mechanics* (Wiley, ed. 2, 1995).

Acknowledgments: We thank Y. Veys, S. van Nieuwstadt, and B. Cruz for contributing to an early phase of design and control work, as well as N. Esparza-Duran for heel manufacturing.

Funding: This work was in part funded by the Caltech Gary Clinard Innovation Fund. We thank M. Gharib and the Center for Autonomous Systems and Technologies for the funding support.

Author contributions: A.R. and S.-J.C. conceived and envisioned a first prototype of LEO, which was developed by A.R. with critical feedback and input from S.-J.C. S.-J.C. directed the research activities that enabled demonstration of the new LEO robot concept reported in the article. K.K. and P.S. designed the robot, and P.S. selected the main components, built the robot hardware, and implemented the software. K.K., P.S., and E.-S.L. contributed to modeling, controller design and stability proof, and performance analysis of LEO with critical feedback and input from S.-J.C. K.K., P.S., E.-S.L., and S.-J.C. designed experiment plans. P.S. and E.-S.L. performed experiments, and K.K., P.S., and E.-S.L. evaluated experimental results. K.K., P.S., E.-S.L., and S.-J.C. prepared and edited the manuscript, and all authors reviewed the manuscript. **Competing interests:** California Institute of Technology filed a U.S. nonprovisional patent application on this work on 23 December 2020. **Data and materials availability:** All data needed to evaluate the conclusions in the paper are present in the paper or the Supplementary Materials.

Submitted 16 December 2020

Accepted 8 September 2021

Published 6 October 2021

10.1126/scirobotics.abf8136

Citation: K. Kim, P. Spieler, E.-S. Lupu, A. Ramezani, S.-J. Chung, A bipedal walking robot that can fly, slackline, and skateboard. *Sci. Robot.* **6**, eabf8136 (2021).

A bipedal walking robot that can fly, slackline, and skateboard

Kyunam Kim, Patrick Spieler, Elena-Sorina Lupu, Alireza Ramezani, and Soon-Jo Chung

Sci. Robot., **6** (59), eabf8136.

DOI: 10.1126/scirobotics.abf8136

View the article online

<https://www.science.org/doi/10.1126/scirobotics.abf8136>

Permissions

<https://www.science.org/help/reprints-and-permissions>